Structural Characteristics and Catalytic Activity of Nanocrystalline Ceria–Praseodymia Solid Solutions

3 AUTHORS, INCLUDING:

Benjaram M Reddy
CSIR-Indian Institute of Chemical Technolo…
279 PUBLICATIONS **5,530** CITATIONS

Structural Characteristics and Catalytic Activity of Nanocrystalline Ceria−Praseodymia Solid Solutions

Benjaram M. Reddy,* Gode Thrimurthulu, and Lakshmi Katta

Inorganic and Physical Chemistry Division, Indian Institute of Chemical Technology, Hyderabad 500 607, India

Yusuke Yamada

Department of Material and Life Science, Graduate School of Engineering, Osaka University, 2-1 Yamada-oka, Suita, Osaka 565-0871, Japan

Sang-Eon Park

Laboratory of Nano-Green Catalysis, Department of Chemistry, Inha University, Incheon 402-751, Republic of Korea

Ceria−praseodymia (CP) nanocrystalline solid solutions were prepared by a coprecipitation method and calcined at various temperatures to understand the thermal effects on the physicochemical properties of the nano-oxides. The structural and redox properties of the synthesized samples were investigated by means of X-ray diffraction (XRD), transmission electron microscopy (TEM-HREM), BET surface area (S_{BET}), Raman spectroscopy (RS), X-ray photoelectron spectroscopy (XPS), UV−visible diffuse reflectance spectroscopy (UV−vis DRS), and temperature programmed reduction (TPR) techniques. The catalytic efficiency toward oxygen storage capacity (OSC) and CO oxidation activity have been investigated. The XRD results confirmed the successful incorporation of praseodymium into the ceria lattice through the formation of nanoscale face-centered cubic solid solutions. The TEM-HREM observations supported the nanocrystalline nature of the solid solutions, as indicated by XRD results. XPS results revealed the presence of cerium and praseodymium in both 3+ and 4+ oxidation states, and surface enrichment of Pr. The UV−vis DRS results revealed an increase of Ce^{3+} species, indicating enhanced reducibility of the ceria upon Pr doping. Raman spectral analysis provided strong evidence for enhanced formation of oxygen vacancies inline with UV−vis DRS results. TPR measurements showed an enhanced bulk reduction at much lower temperatures, indicating increased oxygen mobility in the samples which enable the enhanced oxygen diffusion at lower temperatures. Ceria−praseodymia solid solutions were found to be thermally quite stable, and exhibit high oxygen storage capacity and CO oxidation activity even after calcination at high temperatures.

Introduction

Ceria (CeO_2) has been established as a principal oxide material used in catalytic applications in which oxidation−reduction processes are involved.[1,2] Mainly, the significance of ceria in three-way catalysis (TWC) originates from its remarkable oxygen storage/release capability (OSC) and its ability to undergo rapid and repeatable redox cycles. This feature is strongly related to the easy creation and diffusion of oxygen vacancies, especially at the ceria surface.[1] In TWC, ceria transforms three environmentally hazardous gases, namely, CO, NO_x, and hydrocarbons, into environmentally benign or less hazardous forms.[3−5] Besides, many technological and bioapplications have also been benefited from the unique redox and OSC properties of the ceria.[6] However, despite its wide applicability, pure ceria is associated with some drawbacks like thermal sintering and deactivation of the redox couple, which result in the decline of OSC and catalytic activity.[7−9] Therefore, improved oxygen storage materials are considered necessary owing to the demand for increasingly better catalytic perfor-

mance and durability. Hence, several efforts have been directed toward eliminating the drawbacks of ceria by doping with other isovalent/aliovalent cations.[10,11] The isovalent cations frequently employed are Zr^{4+}, Hf^{4+}, Ti^{4+}, etc., and the aliovalent cations are La^{3+}, Sm^{3+}, $Mn^{2+/3+}$, $Fe^{2+/3+}$, Eu^{3+}, Tb^{3+}, Pr^{3+}, and others.[1,6,11−17]

In many cases, the redox properties and chemical activity of pure ceria could be enhanced by introducing dopant cations into the oxide lattice. A clear physical picture of the connection between the choice of a dopant and the OSC in ceria is still lacking.[6] The OSC is strongly linked to the easy formation and mobility of vacancies, and diffusion of oxygen ions from bulk to surface, and vice versa.[18] The introduction of smaller isovalent Zr^{4+} could obviously enhance OSC by decreasing the Ce^{4+}/ Ce^{3+} reduction energy, preserving oxygen defects, and retarding OSC degradation at high temperatures.[8,19,20] However, zirconium introduction did not introduce a significant number of oxygen vacancies,[21,22] whereas doping of aliovalent nonreducible cations into the lattice of CeO_2−ZrO_2 or CeO_2 was reported to decrease the activation energy of oxygen release by spontaneously generating a great amount of both delocalized (mobile) and some highly localized oxygen vacancies around dopant cations.[23−26]

* To whom correspondence should be addressed. E-mail: bmreddy@iict.res.in; mreddyb@yahoo.com.

Nanocrystalline Ceria−Praseodymia Solid Solutions

J. Phys. Chem. C, Vol. 113, No. 36, 2009 **15883**

Further, the high energies associated with the vacancies of the trivalent dopant ions would prevent long-range ordering of the vacancies,[26] and effectively "trap" the oxygen vacancies. This would hinder further decrease of activation energy for oxygen ion diffusion through the bulk lattice.[5]

As reported, small ionic size and low valence states of dopants have shown various effects on the physicochemical properties such as the number of vacancies and defect reaction energies.[7,8] Recently, considerable attention has been paid to introducing variable valence ions into the ceria lattice to recognize their role in defect chemistry. The oxygen atoms/vacancies attached to reducible elements are mobile, which could contribute to the OSC of mixed oxides.[25,27] Among the reducible elements, praseodymium is particularly suitable for making a solid solution with ceria. The structure of Pr_6O_{11} is fluorite type, and the ionic radius of Pr^{4+} ions is close to that of Ce^{4+} ions.[27] In the mixed oxide, it can form mixed valence states of Pr^{3+} and Pr^{4+} under ambient conditions and facilitate oxygen vacancies. Further, in ceria−praseodymia solid solutions, both elements have 3+ and 4+ oxidation states that are readily formed, and the anion vacancy would be very much mobile in this system.[26] In order to gain more insight into the properties of Ce−Pr solid solutions, especially with respect to oxygen vacancies, OSC, and redox properties, we have prepared Ce−Pr solid solutions and investigated their structural and redox properties using X-ray diffraction (XRD), transmission electron microscopy (TEM-HREM), BET surface area (S_{BET}), X-ray photoelectron spectroscopy (XPS), UV−visible diffuse reflectance spectroscopy (UV−vis DRS), Raman spectroscopy (RS), and temperature programmed reduction (TPR) techniques. The oxygen storage/release capacities of solid solutions and catalytic activity toward CO oxidation have also been evaluated.

Experimental Section

Ceria−praseodymia (CP, 80:20 mol % based on oxides; $Ce_{1−x}Pr_xO_{2−\delta}$, $x = 0.2$) solid solution was prepared by adopting a coprecipitation method from ultrahigh dilute solutions using $Ce(NO_3)_3 \cdot 6H_2O$ and $Pr(NO_3)_3 \cdot 6H_2O$ precursors. The requisite amounts of the precursors were dissolved separately in double-distilled water under mild stirring conditions and mixed together. Upon complete mixing, excess ammonium hydroxide was added dropwise until the precipitation was complete (pH ∼8.5). The resulting slurry was filtered off and thoroughly washed with distilled water until free from anion impurities. The accumulated mixed oxide/hydroxide paste was carefully placed and covered in a clean ceramic crucible and allowed to dry overnight in a hood. It was then oven-dried at 393 K for 12 h to remove water and any residual precursors remaining from the coprecipitation step. Finally, it was calcined at 773 K for 5 h in air atmosphere. To understand the thermal effect on the physicochemical properties of the samples, the finished sample was heated once again at 873, 973, and 1073 K, respectively, for 5 h. After cooling, the solid residues were ground until they were fine powders and stored. Pure cerium oxide was also prepared for comparison purposes by adopting the same precipitation method.[28]

Powder X-ray diffraction patterns were recorded on a Rigaku Multiflex instrument using a nickel-filtered Cu Kα (0.15418 nm) radiation source and a scintillation counter detector. The intensity data were collected over a 2θ range of 2−80° with a 0.02° step size and using a counting time of 1 s per point. The XRD phases present in the samples were identified with the help of Powder Diffraction File-International Center for Diffraction Data (PDF-ICDD). The average crystallite size of the oxide phases was estimated with the help of the Debye−Scherrer equation using the XRD data of all prominent lines, and the lattice parameter was calculated by a standard cubic indexation method using the intensity of the most prominent peak (111).

The BET surface areas were determined by N_2 physisorption at liquid N_2 temperature on a Micromeritics Gemini 2360 instrument. Prior to analysis, the samples were oven-dried at 393 K for 12 h and flushed with argon gas for 2 h. The electron microscopy studies were made on a JEM-2010 (JEOL) instrument equipped with a slow-scan CCD camera at an accelerating voltage of 200 kV. Samples were sonically dispersed in ethanol and deposited on a carbon coated copper grid before examination.

Raman spectra of the samples were obtained by using a LabRam HR800UV Raman spectrometer (Horiba Jobin-Yvon) equipped with a confocal microscope and liquid-nitrogen-cooled charge-coupled device (CCD) detector. The exciting laser wavelength of 325 nm from a He−Cd laser (Melles Griot Laser) was focused on the sample under the microscope, with the diameter of the analyzed spot being ∼1 μm. The scanning range was $200−1200$ cm^{-1} with the accuracy of 1 cm^{-1}.

The X-ray photoelectron spectroscopy measurements were made on a Shimadzu (ESCA 3400) spectrometer by using Mg Kα (1253.6 eV) radiation as the excitation source. Charging of catalyst samples was corrected by setting the binding energy (BE) maximum of the adventitious carbon (C 1s) at 284.6 eV.[6,29] The XPS analysis was done at room temperature, and pressures were typically on the order of less than 10^{-8} Pa. The samples were outgassed in a vacuum oven overnight before XPS measurements. Quantitative analysis of atomic ratios was accomplished by determining the elemental peak areas, following the Shirley background subtraction.[6,29]

The UV−vis DRS measurements were performed over the wavelength range 200−800 nm using a GBS-Cintra 10e UV−vis NIR spectrophotometer with an integration sphere diffuse reflectance attachment. Samples were diluted in a KBr matrix by pelletization.

The reducibility of the catalysts was studied by temperature programmed reduction. About 100 mg of catalyst sample was loaded in an isothermal zone of the reactor and heated at a rate of 10 K min^{-1} to 473 K in 30 mL min^{-1} helium gas, which facilitated desorption of the physically adsorbed water. After the sample was cooled to room temperature, the helium was switched to 20 mL min^{-1} of reducing gas consisting of 5% H_2 in argon and the temperature was increased to 1073 K at a heating rate of 5 K min^{-1}. The reactor effluent gas was passed through a molecular sieve trap to remove the produced water and was analyzed by gas chromatography (GC) using a thermal conductivity detector (TCD), and the reduction of CuO to metallic copper was used for calibration purposes.

The OSC was determined by the oxygen release characteristics of the sample in the temperature region 573−1073 K with the help of the thermogravimetric method. The change in the weight of the sample was monitored by thermogravimetry (TG) under cyclic heat treatments in flowing nitrogen or dry air. A commercial Netzsch TG-DTA analyzer (Luxx, STA, 409 PC, Germany) was employed for this purpose. The heat cycle consisted of heating the sample to 1073 K, cooling to 423 K, and again heating to 1073 K. All heating and cooling rates were 5 K min^{-1}. The weight loss of the sample during the second heating cycle was used to measure the oxygen release properties. This standard method is essentially similar to the one reported by Ozawa et al.[30] Further studies are under active progress to evaluate the role of heating rate on the OSC properties of the oxide materials.
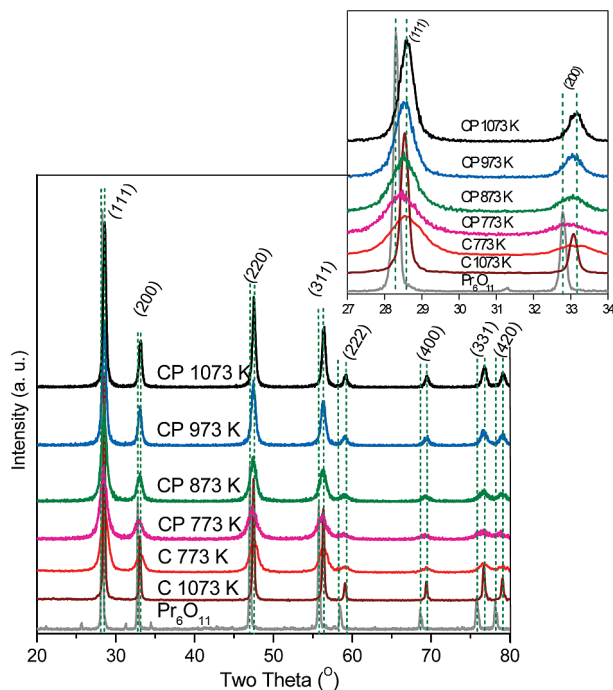
Figure 1. Powder XRD patterns of ceria–praseodymia samples calcined at various temperatures along with ceria calcined at 773 and 1073 K and praseodymium oxide (Pr_6O_{11}).

The catalytic activity of the synthesized solid solutions was evaluated for the oxidation of CO at normal atmospheric pressure and temperatures in the range 300–773 K in a fixed bed microreactor at a heating ramp of 5 K min^{-1}. About 100 mg of catalyst sample (250–355 μm sieve fraction) diluted with quartz particles of the same sieve fraction was placed in a quartz reactor for evaluation. The temperature was measured directly at the catalyst bed, using a thermocouple placed in the hollow part of the reactor. The following gases and gas mixtures were used (supplied by Air Liquide): argon (>99.999% purity), 9.98% CO in argon (CO purity, >99.997%; argon purity, >99.99%), and 10.2% O_2 in argon (oxygen purity, >99.995%). The total flow rates maintained by three mass flow controllers were in the range 50–60 N mL min^{-1} (milliliters normalized to 273.15 K and 1 atm.). The CO and CO_2 gas concentrations were measured using an Uras 14 infrared analyzer module, and the O_2 concentration was measured using a Magnos 16 analyzer (Hartmann & Braun). Prior to oxidation of CO, the catalysts were heated to 773 K in a 10.2% O_2/Ar gas mixture, using a heating ramp of 10 K min^{-1}, and kept at the final temperature for 1 h. The oxidized sample was then purged in argon and cooled to the desired starting temperature. The CO/O_2 reactant feed ratio was 1, and partial pressures of CO and O_2 were in the range of 10 mbar.

Results and Discussion

X-ray powder diffraction patterns of ceria–praseodymia (CP) solid solution and CeO_2 (C) calcined at various temperatures from 773 to 1073 K at the intervals of 100 K, along with praseodymium(3+/4+) oxide (Pr_6O_{11}, Aldrich Chemicals), are presented in Figure 1. The diffraction patterns of CeO_2 and Pr_6O_{11} are associated with defective face-centered cubic (fcc) structure (PDF-ICDD 34-0394 and PDF-ICDD 42-1121, respectively). The corresponding diffraction peaks of both of the samples are very similar to each other, because the ionic radii of Ce^{4+} (0.97 Å) and Pr^{4+} (0.96 Å) are very close to each other.

Therefore, the enlarged diffraction patterns in the 2θ range from 27 to 34° are shown as the inset in Figure 1. The XRD patterns of CP samples exhibited only the reflections typical of (111), (200), (220), (311), (222), (400), (331), and (420) planes corresponding to the characteristic defective structure of the cubic CeO_2.[31] Further, these reflections were thermally stable without any phase segregation even after calcination at 1073 K. This result indicates that praseodymium ions are completely incorporated into the ceria lattice, thereby forming thermally stable solid solutions. There is a slight shift in the diffraction peaks of the Ce–Pr patterns toward lower angles when compared to that of pure ceria. This corresponds to an increase of the lattice parameter (shown in Table 1), which can be attributed to the presence of Pr^{3+} along with Pr^{4+} in the oxide lattice. The ionic radius of Pr^{3+} (1.13 Å) is slightly larger than that of Ce^{4+} (0.97 Å) and nearly equal to Ce^{3+} (1.14 Å). Therefore, a slight lattice expansion can be expected due to the substitution of Ce^{4+} by Pr^{3+} and/or the increase of Ce^{3+} ions in the solid solution.[1] This observation is in agreement with Vegard's law, which holds that a linear relationship exists, at a constant temperature, between the crystal lattice parameter of an alloy and the concentrations of its constituent elements. The obtained lattice parameter values for the $Ce_{1-x}Pr_xO_{2-\delta}$ solid solution agree well with the literature reports.[32,33] Additionally, we observed a small decrease in the lattice parameter values with increasing calcination temperature from 773 to 1073 K. We therefore deduce that a comparatively high amount of Pr^{3+} is present in the 773 K calcined sample and generates a proportional amount of oxygen vacancies by the charge neutrality mechanism. Apparently, at higher calcination temperatures, some amount of Pr^{3+} was converted to Pr^{4+}, resulting in the consequent decrease of lattice parameter and amount of oxygen vacancies.[6,34] The XRD peaks corresponding to the CP sample become narrow with increasing calcination temperature due to an increase in average crystallite size. The average crystallite size increased from ∼7 to ∼10 nm at 773 and 873 K, respectively, and reached ∼16 nm at 1073 K, indicating that the crystallization of CP was accelerated above 873 K. This result is in agreement with the BET surface area values shown in Table 1. The nanocrystalline Ce–Pr samples exhibited a high BET surface area of 72 and 31 m^2 g^{-1} for 773 and 1073 K calcined samples, respectively. The decline of the specific surface area with increasing calcination temperature could be due to the increase in the particle size with temperature.

The surface morphology and structural properties of CP samples were examined by the TEM-HREM technique. The corresponding micrographs of 773 and 1073 K calcined samples are shown in Figures 2 and 3, respectively. The obtained TEM micrographs reveal that the samples bear agglomerated microstructures with octahedral particulates. As observed from Figures 2a and 3a (encircled area), the particulates are poorly visible at low calcination temperatures and are clearly visible and dominated at higher calcination temperatures. HREM images showed that the sample is in polycrystalline form and constituted by small crystallites. The crystallites are randomly oriented toward each other with an average particle size of ∼7 nm which increased to ∼16 nm, after an increase of the calcination temperature from 773 to 1073 K. These results are in good agreement with those obtained from XRD peak broadening measurements. All of the crystallites are oriented along the [011] crystallographic direction,[35] and the labeling of the crystal planes for each particle is indicated in Figure 3b. The shape of most crystallites is compatible with an octahedron predominately enclosed by {111} planes at 3.1 Å, and there is also the presence

Nanocrystalline Ceria−Praseodymia Solid Solutions

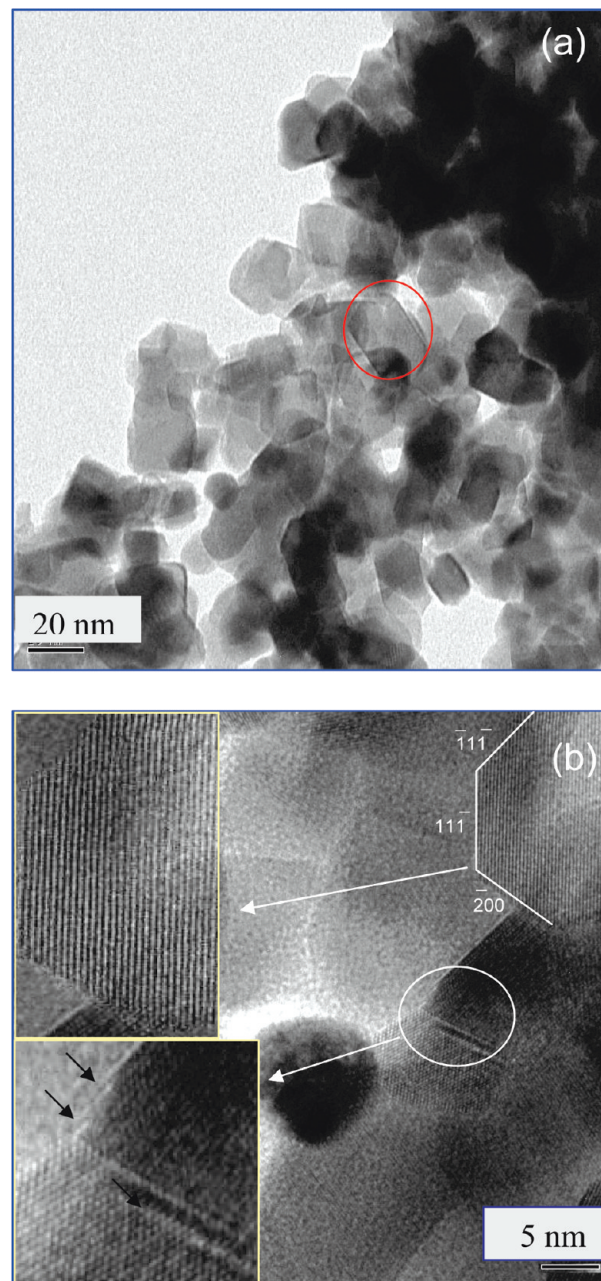*J. Phys. Chem. C, Vol. 113, No. 36, 2009* **15885**

TABLE 1: BET Surface Area (*S*), Average Crystallite Size (*D*), Lattice Parameter (*a*), OSC, Surface Composition, and Ce/Pr Atomic Ratio of Ceria and Ceria−Praseodymia Solid Solutions Calcined at Different Temperatures

sample	S (m^2 g^{-1})	D^b (nm)	a^b (Å)	OSC μmol of O$_2$/g of ceria	surface composition^a (mol %) Ce	Pr	Ce/Pr atomic ratio^a
C 773	41	7.3	5.410	40.5			
CP 773	72	7.1	5.430	210.0	55.6	44.4	1.253
CP 873	59	10.4	5.421		55.6	44.4	1.253
CP 973	42	14.8	5.419		55.4	44.6	1.242
CP 1073	31	16.3	5.415		55.5	44.5	1.247

^{a} From XPS analysis. ^{b} From XRD analysis.
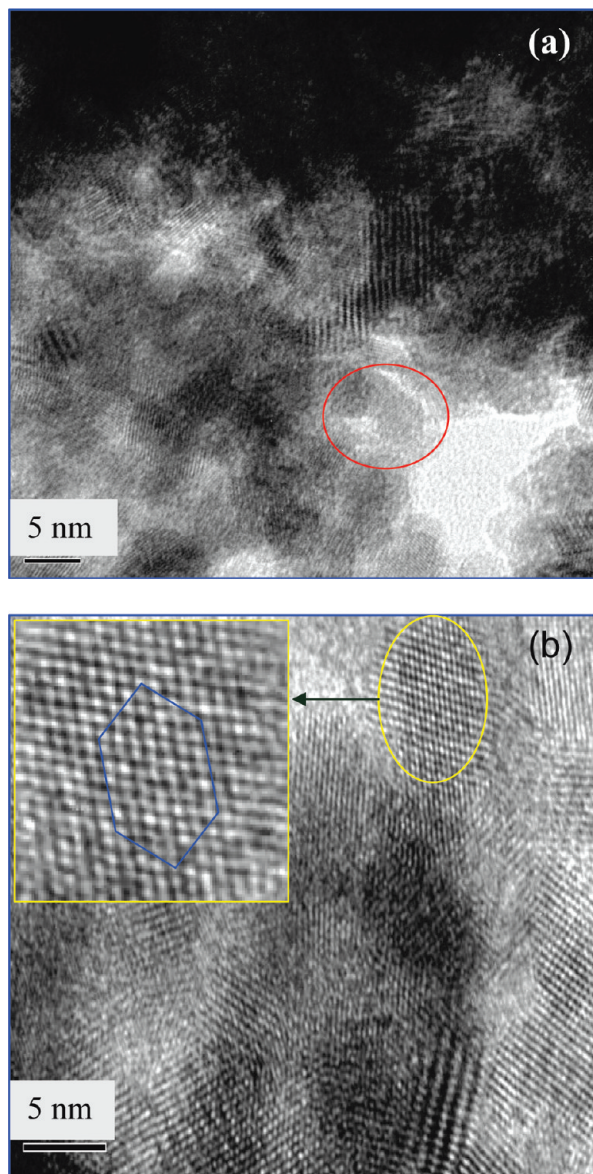
Figure 2. TEM (a) and HREM (b) micrographs of the ceria−praseodymia sample calcined at 773 K.

Figure 3. TEM (a) and HREM (b) micrographs of the ceria−praseodymia sample calcined at 1073 K.

of less stable {200} planes at 2.7 Å. On the faces and terrace of the crystallites, the presence of some steps and overlapping regions of crystallites (inset of Figure 3b) is observed which could be responsible for the better catalytic activity even after higher calcination temperatures.

Raman spectroscopy is one of the most useful techniques for characterization of catalytic materials and to gather information on both the M−O bond arrangement and lattice defects. It is well-known in the literature that the intensity of Raman bands

may vary depending on the laser source used. Recently, there was a report on the investigation of the surface and bulk properties of ceria-based materials with four different excitation lasers by Raman spectroscopy.[36] On the basis of the fact that the laser with shorter wavelength is closer to the electronic absorption of samples, it was reported that the Raman informa-
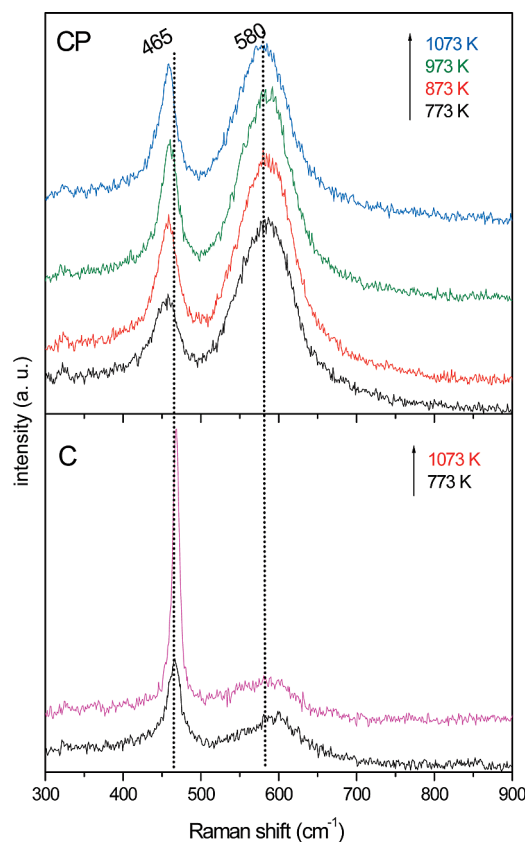
Figure 4. Raman spectra of ceria−praseodymia and ceria samples calcined at various temperatures.

Figure 5. Variations in the intensity ratio of Raman bands at 580 and 465 cm^{-1} and loss of oxygen vacancies (%) of ceria−praseodymia and ceria samples with increasing calcination temperature.

tion detected by excitation laser with shorter wavelength is more sensitive to the surface region of the samples. We have used a UV excitation laser (He−Cd laser) with a wavelength of 325 nm in the present investigation. Moreover, in the present investigation, the synthesized samples showed strong absorption in the UV region, as observed from the UV−vis DRS method discussed in the later paragraphs. Therefore, it can be stated that the bands corresponding to the oxygen vacancy formation in the oxides are related to the surface region. Raman spectra of the CP and ceria samples calcined at various temperatures are shown in Figure 4. All samples revealed two main peaks in the region 450−650 cm^{-1}, and the peak at 465 cm^{-1} has been related to the F_{2g} vibrational mode, characteristic of the cubic fluorite structure according to McBride et al.[37] It can be viewed as a symmetric breathing mode of oxygen atoms of the CeO_8 unit of the ceria lattice. The peak at 580 cm^{-1} was attributed to lattice defects, resulting from the formation of oxygen vacancies, which will allow this mode of vibration by relaxation of the selection rules.[37] As can be noted from Figure 4, this peak is less prominent in the case of ceria samples, while it became more strong in the CP samples. It could be due to the formation of more oxygen vacancies to compensate charge balance for the presence of Pr^{3+} and the increased Ce^{3+} ions. It is also observed that the characteristic F_{2g} vibrational mode is shifted to lower frequencies and broadened when the Pr cations were introduced into the ceria lattice. This peak is gradually sharpened with a small red shift with increasing calcination temperature. According to Hernandez et al.,[1] these observations could be explained by several factors, such as phonon confinement, strain, inhomogeneity of the size distribution, defects, and variations in phonon relaxation with the particle size that may contribute to the changes in the position and line width of the F_{2g} mode Raman peak. In CeO_{2-x}, the combined effects of strain and
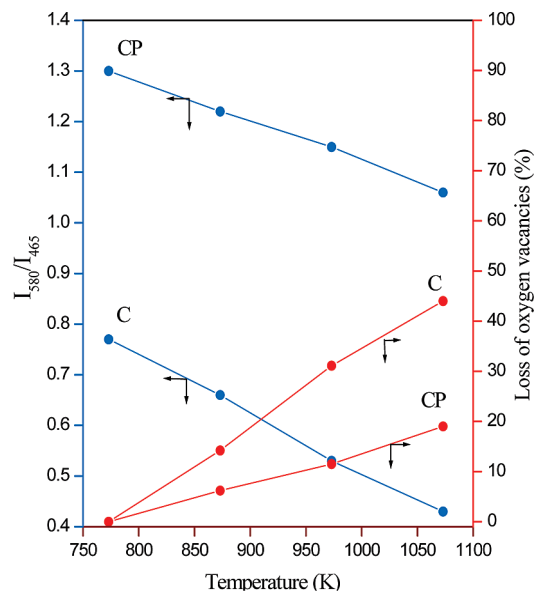
phonon confinement have been used to explain why the Raman peak at 464 cm^{-1} progressively shifts to lower energies, broadens, and becomes asymmetric when the ceria particle size gets smaller.[1] These previous observations are in good agreement with the Raman and XRD results of the present Ce−Pr-oxide system.

The difference in the temperature dependence of defect concentration in ceria−praseodymia is quite striking. The ratio between the intensities of 580 and 465 cm^{-1} Raman bands has been related to the concentration of oxygen vacancies in the materials, and it was noted that the higher the I_{580}/I_{465} ratio, the higher the oxygen vacancies.[38] The relationship between I_{580}/I_{465} and the calcination temperature for ceria and Ce−Pr samples is presented in Figure 5. It can be observed from this figure that the incorporation of Pr into the ceria lattice increases the vacancy concentration by about 3 times due to the generation of vacancies for charge compensation as a result of the presence of Pr^{3+} and the increased Ce^{3+} ions. Moreover, ceria exhibits a significant loss of oxygen vacancies (∼45%) as a function of increasing calcination temperature, whereas the ceria−praseodymia solid solution shows a moderate decrease (∼20%). This observation confirms the enhanced stability of oxygen defects against thermal aging by the incorporation of Pr into the ceria lattice. We propose that the enhanced stability and number of oxygen defects may account for the improved oxygen storage capacity, better CO oxidation activity (explained in the latter paragraphs), and thermal stability of the ceria−praseodymia system compared to pure ceria.

The composition, the chemical states of Ce and Pr ions, and the nature of oxygen present in the samples were examined by the XPS technique. The O 1s core level XPS profiles of the Ce−Pr-oxide sample calcined at different temperatures are presented in Figure 6. It is obvious from the figure that, in addition to the main feature at 531.0 eV, one can detect a pronounced shoulder in the O 1s core level at the high BE side.[29,39] The former one could be attributed to the lattice oxygen associated with the Ce−Pr-oxides and the latter to the absorbed oxygen species (presumably from absorbed water and/or carbonates).[6] Figure 7 typically demonstrates the XPS spectra of the Ce 3d core level for Ce−Pr-oxide solid solution calcined at
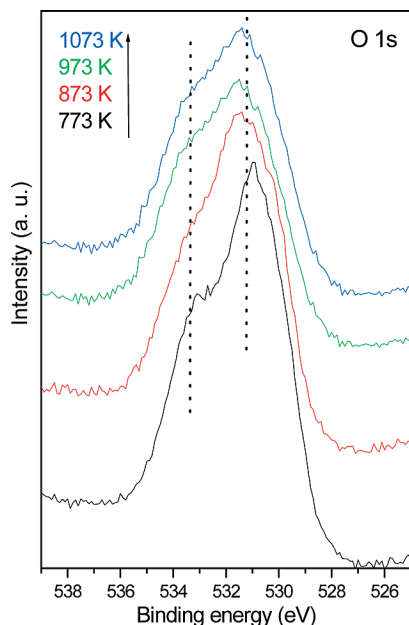
Nanocrystalline Ceria−Praseodymia Solid Solutions

J. Phys. Chem. C, Vol. 113, No. 36, 2009 **15887**

Figure 6. O 1s XPS patterns of ceria−praseodymia samples calcined at various temperatures.
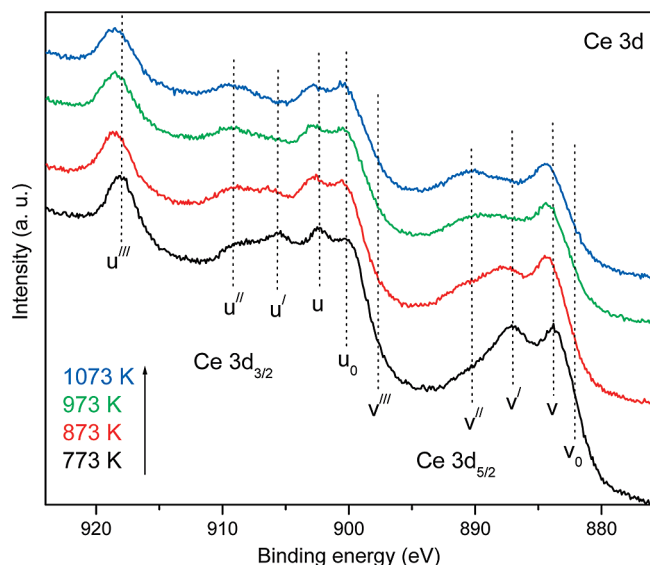

Figure 7. Ce 3d XPS patterns of ceria−praseodymia samples calcined at various temperatures.

different temperatures. The complex Ce 3d level spectrum exhibited an overlap among a series of peaks in the range 880−920 eV due to the hybridization of the O 2p valence band with the Ce 4f level, and the electron binding values agree well with the reported results of cerium oxides.[40,41] In Figure 7, the Ce $3d_{3/2}$ and Ce $3d_{5/2}$ ionization features have been labeled according to the published XPS analyses of CeO_2 that the bands u_0 and u with u′, u″, and u‴ satellite bands are attributed to the Ce $3d_{3/2}$ ionization, while the bands v_0 and v with v′, v″, and v‴ satellites to the Ce $3d_{5/2}$ ionization.[35] The bands labeled u (902.3 eV) and v (883.7 eV) are the main lines, whereas u″ (909.1 eV), u‴ (917.9 eV), v″ (890.1 eV), and v‴ (897.5 eV) are the satellites related to Ce^{4+} ions. The main signals labeled v_0 (882 eV) and u_0 (899 eV) and the satellites u′ (905.6 eV) and v′ (887.1 eV) are ascribed to Ce^{3+}. However, peak intensities corresponding to Ce^{3+} are relatively weak compared to that of the Ce^{4+}. Since the concentrations of Ce^{3+} and Ce^{4+} are in relative proportion to the intensity of emission, analysis of the
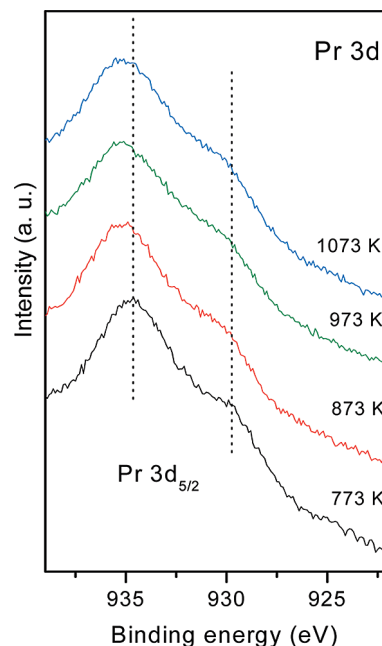

Figure 8. Pr 3d XPS patterns of ceria−praseodymia samples calcined at various temperatures.

peaks associated with the representative Ce^{3+} and Ce^{4+} features suggests that cerium is present at the surface in both 4+ and 3+ oxidation states and the major valence of cerium in Ce−Pr-oxide is 4+. Moreover, with increasing calcination temperature, the relative intensity of u′ and v′ annotated peaks decreased, indicating the decrease in the surface content of Ce^{3+} and a proportional amount of oxygen vacancies in agreement with the Raman results.

Figure 8 shows Pr 3d core level XPS spectra of the CP sample calcined at various temperatures. In order to identify the different oxidation states of Pr ions in the samples, it is necessary to fit the Pr 3d spectra with contributions from the two possible oxidation states of Pr (3+ and 4+). Pr 3d spectra exhibited a rather similar shape like the Ce 3d spectra of Ce(3+)/Ce(4+) compounds. However, in comparison to Ce 3d, the Pr 3d spectra are not studied extensively in the literature. The Pr 3d spectra consist of two sets of spin−orbit multiplets at binding energies of ∼933 and ∼953 eV which correspond to $3d_{5/2}$ and $3d_{3/2}$, respectively.[42] The $3d_{3/2}$ sublevel presents complex features due to the multiplet effect, while the $3d_{5/2}$ sublevel consists of two features corresponding to two possible oxidation states (Pr^{3+} and Pr^{4+}).[43] Therefore, we have undertaken the Pr $3d_{5/2}$ region to understand the oxidation states of praseodymium. The spectra obtained show a pronounced shoulder at 929.7 eV and a maximum at 934.5 eV. According to the previous results, we assigned the former to Pr^{3+} and the latter to Pr^{4+}.[38] This indicates that the prepared sample contains both 3+ and 4+ oxidation states of praseodymium at the surface region. With increasing calcination temperature, the intensity of the low energy shoulder seems to decrease slightly, suggesting a lower Pr^{3+} contribution after severe calcination.

Table 1 also shows the composition, and the atomic ratios for Ce and Pr in the surface region of the ceria−praseodymia solid solution calcined at various temperatures. It is clear from the table that the content of Pr in the surface region is ∼44% which is higher than that of the nominal content of 20%, while the content of Ce is ∼55% which is lower than that of the nominal content of 80%. This observation indicates an enrichment of Pr in the surface region of the CP sample. It is also

known that segregation of dopant cations at the surface and domain boundaries of ceria samples is a well-known established phenomenon. In the present study, the Pr enrichment is superior to that of the reported value (Pr content of 35% for $Ce_{1-x}Pr_xO_{2-\delta}$, $x = 0.2$) by Luo et al.[36] The possible reason could be the variation in the preparation method, since the method of preparation significantly influences the properties of the resulting materials. Further, the surface composition also did not change considerably when the temperature was increased from 773 to 1073 K.

The UV–vis DRS technique has been used extensively to study various metal oxides to obtain information on the changes in the bulk, surface coordination, and different oxidation states of the ions by measuring d–d and f–d transitions, and oxygen–metal ion charge transfer bands.[44] The deconvoluted UV–vis DR spectrum of the CP sample calcined at 773 and 1073 K and ceria at 773 K are shown in Figure 9. Pure ceria (773 K calcined) exhibits three absorption maxima in the UV region centered at ∼255, 285, and 340 nm. The former two bands correspond to $Ce^{3+} \leftarrow O^{2-}$ and $Ce^{4+} \leftarrow O^{2-}$ charge transfer transitions, respectively, and the latter are assigned to interband transitions.[45] Besides, CP samples showed one more intense absorption band in the visible region (400–650 nm) which is associated with Pr^{3+} ion transitions.[38] It can be seen that the CP samples show a distinctive blue-shift of the adsorption edge (interband transition) as compared to that of ceria. This could be due to the presence of Pr^{3+} ions in the system which provoke a significant increase in the Ce^{3+} fraction on the surface, thereby increasing the charge-transfer gap between the O 2p and Ce 4f orbitals and inducing the blue-shift in the absorption edge.[1] Moreover, the characteristic $Ce^{3+} \leftarrow O^{2-}$ charge transfer band is also well resolved in the case of Ce–Pr samples. These results imply the occurrence of oxygen vacancy defects in the samples corroborating with the Raman spectroscopy studies.

H_2-TPR experiments were performed to analyze the redox properties of ceria and CP samples calcined at 773 and 1073 K. The corresponding TPR profiles are shown in Figure 10. Ceria shows two typical characteristic reduction peaks; the low temperature peak is assigned to the easily reducible surface-capping oxygen (≈807 K), whereas the high temperature peak is due to the removal of bulk oxygen (≈1168 K not shown in the figure). The incorporation of Pr into the ceria lattice strongly modified the reduction behavior of ceria by shifting surface and bulk reduction to lower temperatures. For the 773 K calcined sample, the corresponding temperatures are 727 and 774 K, respectively. It is interesting to note that the bulk reduction temperature was much lowered compared to that of ceria. One possible reason for this behavior is the enhancement of oxygen vacancies (as evidenced from RS results) which increases the oxygen mobility in the lattice. Moreover, it is known that Pr addition induces ordered arrangements of vacancies,[26] thereby creating a pathway for oxygen diffusion. This would promote the oxygen ion diffusion from the bulk to the surface, enabling the bulk reduction at low temperatures.

The oxygen storage/release property of ceria is the most important factor which contributes to the catalytic activity of ceria in oxidation reactions. The OSC of ceria relies on transport properties like oxygen diffusion at the surface and/or in the bulk of oxides, which will help in the understanding of the CO oxidation activity of ceria. Oxygen diffusion is mainly determined by the presence, concentration, and mobility of lattice defects (such as oxygen vacancies).[5] The present ceria–praseodymia system exhibited a high OSC of 210 μmol of O_2/g of ceria (167
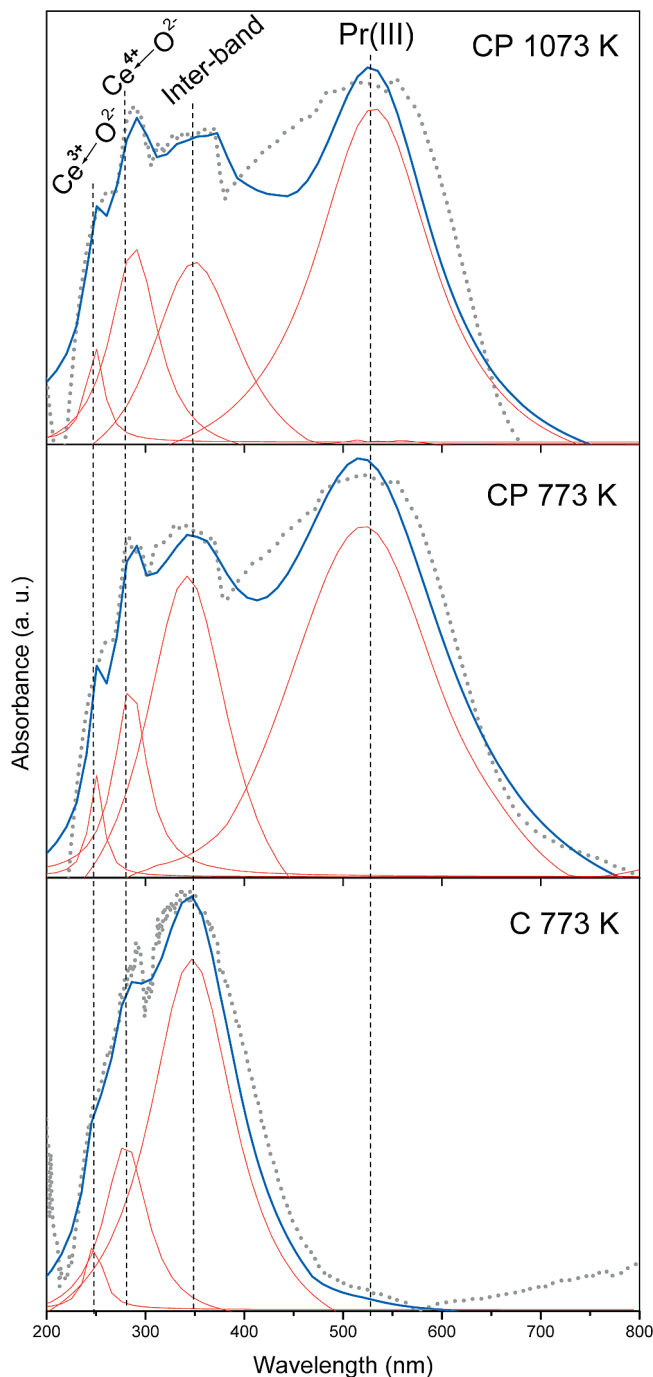

Figure 9. Deconvoluted UV–vis DR spectrum of ceria and ceria–praseodymia samples calcined at different temperatures.

μmol of O_2/g of Ce–Pr-oxide), which is 5 times more than that obtained for the pure ceria sample.[46] The incorporation of Pr into the ceria lattice increased the bulk reduction, and the oxygen atoms bonded to both Ce and Pr (reducible elements) can contribute to the OSC.[27] Moreover, due to the possible valence change of both the ions from 3+ to 4+ or from 4+ to 3+, the up–down swings of the oxygen defects accompanied with the valence change was achieved. Thus, it will have a high diffusivity of oxygen and the ability to store more oxygen as well. Hence, the high OSC of ceria–praseodymia is due to the simultaneous presence of mobile oxygen vacancies and corresponding RE^{4+}/RE^{3+} (RE = Ce and Pr) redox couples.

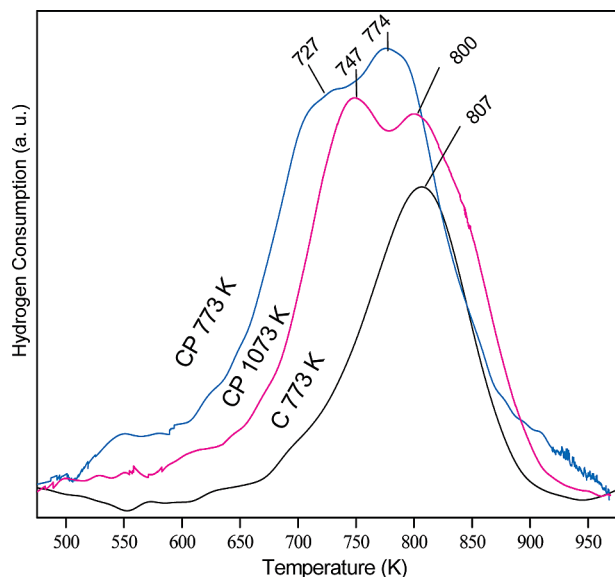The catalytic activities for CO oxidation of Ce–Pr-oxide samples calcined at 773 and 1073 K are presented in Figure

Figure 10. H$_2$-TPR profiles of ceria and ceria−praseodymia samples calcined at different temperatures.
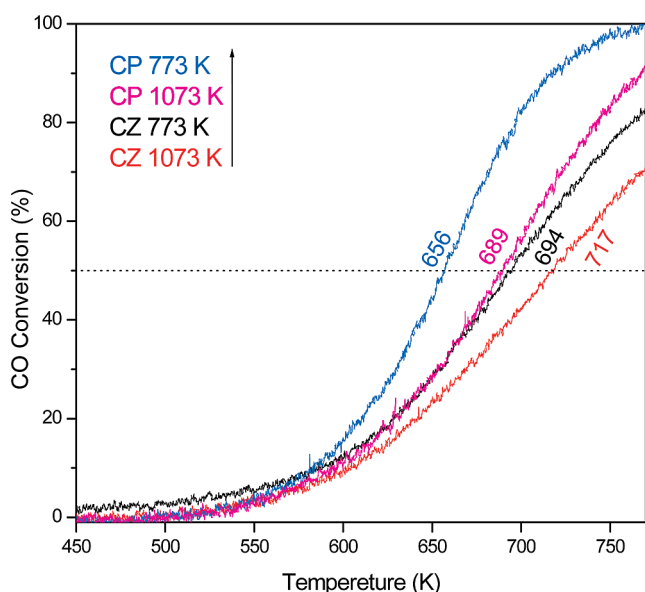

Figure 11. Conversion of CO over ceria−zirconia (CZ) and ceria−praseodymium (CP) samples calcined at 773 and 1073 K as a function of reaction temperature.

11. For comparison purposes, the results for respective ceria−zirconia (CZ) solid solutions (1:1 mol ratio) are also included in the figure. It is well-known that Ce−Zr-oxide solid solutions are superior to pure ceria in terms of stability and catalytic activity for various reactions.[6,28,46,47] Therefore, we preferred to compare the present CP catalyst system with the Ce−Zr-oxide solid solutions. The details of its preparation and structural characteristics could be found from our earlier reports.[28,46] It is evident from Figure 11 that the CP solid solutions exhibited better activity in terms of total conversion as well as light-off temperature (50% conversion). The Ce−Pr-oxide sample calcined at 773 and 1073 K exhibited ∼100 and 90% conversion, respectively. On the other hand, the Ce−Zr-oxide solid solutions provided 85 and 70% conversion for the 773 and 1073 K calcined samples, respectively. The CP oxide sample exhibited light-off temperatures of 656 and 689 K for the 773 and 1073 K calcined samples, respectively. The CZ combination showed the light-off temperatures of 694 and 717

K for the 773 and 1073 K calcined samples, respectively. Since oxygen for this reaction comes from the bulk of the solid solutions, its availability and diffusion energy are greatly influenced by the total conversion and light-off temperature. Unlike Ce−Zr-oxide solid solutions where bulk reduction is associated with a change in the valence state of Ce, the bulk reduction of Ce−Pr-oxide involves both Ce and Pr; therefore, the amount of oxygen that is available for the reaction is increased. It has been reported that oxygen adsorption proceeds directly on the noble metal cluster or on the support, in particular at oxygen vacancies, where the O$_2$ molecule is activated to react with an adsorbed CO molecule.[5] It is interesting to note that the CZ sample exhibited a lesser number of surface oxygen vacancies (the I_{580}/I_{465} value is 1.12 at 773 K and 0.90 at 1073 K with a loss of 22%, not shown in Figure 5), while the CP sample showed a higher number of surface oxygen vacancies (the I_{580}/I_{465} value is 1.3 at 773 K and 1.06 at 1073 K with a loss of 20%, shown in Figure 5), as observed from Raman analysis which enabled the oxygen ion diffusion from the bulk to the surface in the CP solid solutions at lower temperatures. The presence of mobile vacancies and an enhanced amount of reducible oxygen has an important effect on the observed activity for the CO oxidation reaction of Ce$_{1−x}$Pr$_x$O$_{2−\delta}$ solid solutions.

Conclusions

Nanoscale Ce−Pr-oxide solid solutions with high specific surface area have been successfully synthesized by using the coprecipitation method from cerium and praseodymium nitrates as precursors. The XRD results confirmed the formation of thermally stable Ce−Pr-oxide solid solutions with a cubic phase of fluorite structure. S_{BET} and TEM-HREM results indicated that incorporation of Pr into CeO$_2$ results in an increase in the surface area and the formation of nanocrystalline solid solutions of ∼7 nm size. With increasing calcination temperature, a small decrease in surface area and an increase of particle size has been observed. XPS results revealed the existence of cerium and praseodymium in both 3+ and 4+ chemical valence states and segregation of Pr at the surface. The praseodymium content at the surface is 44%, as the nominal content in the sample is 20% only. The surface composition is almost constant upon heat treatment from 773 to 1073 K. Raman results disclose a remarkable increase of oxygen vacancies and are found to be thermally stable up to 1073 K. It is also observed that addition of Pr to CeO$_2$ not only increases the oxygen vacancies but also enhances the Ce^{3+} content. The Ce−Pr-oxide solid solution shows enhanced bulk reduction at lower temperatures, indicating a high mobility of oxygen ions in the sample. The Ce−Pr-oxide combination exhibited a high OSC of 210 μmol of O$_2$/g of ceria, indicating its high ability to take up and release oxygen. The OSC performance is 5 times higher than pure ceria. This can be attributed to the simultaneous presence of enhanced mobile oxygen vacancies, easy bulk reduction, and the cooperative redox couple RE^{3+}/RE^{4+} (RE = Ce and Pr). The Ce−Pr-oxide solid solutions also exhibit superior activity toward CO oxidation compared to Ce−Zr-oxide samples. The thermal stability and ability to release a substantial amount of oxygen at relatively low temperatures makes the Ce−Pr-oxide solid solution a potential material for oxygen storage/release and automotive catalytic applications.

References and Notes

(1) Hernandez, W. Y.; Centeno, M. A.; Romero-Sarria, F.; Odriozola, J. A. *J. Phys. Chem. C* **2009**, *113*, 5629, and references therein.

(2) Kaspar, J.; Fornasiero, P.; Hickey, N. *Catal. Today* **2003**, *77*, 419.

(3) Fu, Q.; Saltsburg, H.; Stephanopoulos, M. F. *Science* **2003**, *301*, 935.

(4) Fernandez-Garcia, M.; Martinez-Arias, A.; Hanson, J. C.; Rodriguez, J. A. *Chem. Rev.* **2004**, *104*, 4063.

(5) Trovarelli, A. In *Catalysis by Ceria and Related Materials*; Hutchings, G. J., Ed.; Catalytic Science Series; Imperial College Press: London, 2002; Vol. 2.

(6) Reddy, B. M.; Saikia, P.; Bharali, P.; Yamada, Y.; Kobayashi, T.; Muhler, M.; Grünert, W. *J. Phys. Chem. C* **2008**, *112*, 16393.

(7) Bunluesin, T.; Gorte, R. J.; Graham, G. W. *Appl. Catal., B* **1997**, *14*, 105.

(8) Mamontov, E.; Egami, T.; Brezny, R.; Koranne, M.; Tyagi, S. *J. Phys. Chem. B* **2000**, *104*, 11110.

(9) Mikulova, J.; Rossignol, S.; Barbier, J., Jr.; Duprez, D.; Kappenstein, C. *Catal. Today* **2007**, *124*, 185.

(10) Lopez, A.-B.; Krishna, K.; Makkee, M.; Moulijn, J. A. *J. Catal.* **2005**, *230*, 237.

(11) Reddy, B. M.; Bharali, P.; Saikia, P.; Khan, A.; Loridant, S.; Muhler, M.; Grünert, W. *J. Phys. Chem. C* **2007**, *111*, 1878.

(12) Sinha, A. K.; Suzuki, K. *J. Phys. Chem. B* **2005**, *109*, 1708.

(13) Krishna, K.; Bueno-Lopez, A.; Makkee, M.; Moulijn, J. A. *Appl. Catal., B* **2007**, *75*, 191.

(14) Wilkes, M. F.; Hayden, P.; Bhattacharya, A. K. *J. Catal.* **2003**, *219*, 295.

(15) Machida, M.; Kurogi, D.; Kijima, T. *Chem. Mater.* **2000**, *12*, 3165.

(16) Guangshe, Li.; Richard, L.; Smith, Hiroshi, I., Jr. *J. Am. Chem. Soc.* **2001**, *123*, 11091.

(17) Bernal, S.; Blanco, G.; Cauqui, M. A.; Martin, A.; Pintado, J. M.; Galtayries, A.; Sporken, R. *Surf. Interface Anal.* **2000**, *30*, 85.

(18) Trovarelli, A. *Comments Inorg. Chem.* **1999**, *20*, 263.

(19) Balducci, G.; Kaspar, J.; Fornasiero, P.; Graziani, M.; Islam, M. S. *J. Phys. Chem. B* **1998**, *102*, 557.

(20) Hori, C. E.; Permana, H.; Simon Ng, K. Y.; Brenner, A.; More, K.; Rahmoeller, K. M.; Belton, D. *Appl. Catal., B* **1998**, *16*, 105.

(21) Rodriguez, J. A.; Wang, X.; Hanson, J. C.; Liu, G.; Iglesias-Juez, A.; Fernandez-Garcia, M. *J. Phys. Chem. B* **2003**, *107*, 3535.

(22) Wang, X.; Hanson, J. C.; Liu, G.; Rodriguez, J. A.; Juez, I. A.; Garcia, M. F. *J. Chem. Phys.* **2004**, *107*, 5434.

(23) Rossignol, S.; Mesnard, D.; Gerard, F.; Kappenstein, C.; Duprez, D. *J. Mater. Chem.* **2003**, *13*, 3017.

(24) Vidmar, P.; Fomasiero, P.; Kaspar, J.; Ciubitosa, G.; Graziani, M. *J. Catal.* **1997**, *171*, 160.

(25) Si, R.; Zhang, Y.-W.; Wang, L.-M.; Li, S.-J.; Lin, B.-X.; Chu, W.-S.; Wu, Z.-Y.; Yan, C.-H. *J. Phys. Chem. C* **2007**, *111*, 787.

(26) Ryan, K. M.; McGrath, J. P.; Farrell, R. A.; O'Neill, W. M.; Barnes, C. J.; Morris, M. A. *J. Phys.: Condens. Matter* **2003**, *15*, L49.

(27) Mikulova, J.; Rossignol, S.; Barbier, J., Jr.; Duprez, D.; Kappenstein, C. *Catal. Today* **2007**, *124*, 185.

(28) Reddy, B. M.; Khan, A. *Catal. Surv. Asia* **2005**, *9*, 155.

(29) Wagner, C. D.; Riggs, W. M.; Davis, L. E.; Moulder, J. F. In *Handbook of X-ray Photoelectron Spectroscopy*; Muilenberg, G. E., Ed.; Perkin-Elmer Corporation: Eden Prairie, MN, 1978.

(30) Ozawa, M.; Matuda, K.; Suzuki, S. *J. Alloys Compd.* **2000**, *56*, 303.

(31) Xie, G.-Q.; Luo, M.-F.; He, M.; Fang, P.; Ma, J.-M.; Ying, Y.-F.; Yan, Z.-L. *J. Nanopart. Res.* **2007**, *9*, 471.

(32) Fagg, D. P.; Kharton, V. V.; Shaula, A.; Marozau, I. P.; Frade, J. R. *Solid State Chem.* **2005**, *176*, 1723.

(33) Nauer, M.; Ftikos, C.; Steel, B. C. H. *J. Eur. Ceram. Soc.* **1994**, *14*, 493.

(34) Hungria, A. B.; Martinez-Arias, A.; Fernandez-Garcia, M.; Iglesias-Juez, A.; Ruiz, A. G.; Calvino, J. J.; Conesa, J. C.; Soria, J. *Chem. Mater.* **2003**, *15*, 4309.

(35) Eleonora, A.; Llorca, Boaro, M., Jr.; Trovarelli, A. *J. Catal.* **2005**, *234*, 88.

(36) Luo, M.-F.; Yan, Z.-L.; Jin, L.-Y.; He, M. *J. Phys. Chem. B* **2006**, *110*, 13068.

(37) McBride, J. R.; Hass, K. C.; Poindexter, B. D.; Weber, W. H. *J. Appl. Phys.* **1994**, *76*, 2435.

(38) Pu, Z.-Y.; Lu, J.-Q.; Luo, M.-F.; Xie, Y.-L. *J. Phys. Chem. C* **2007**, *111*, 18695.

(39) Guodong, F.; Changgen, F.; Zhao, Z. *J. Rare Earths* **2007**, *25*, 42.

(40) Normand, F. L.; Fallah, J. E.; Hilaire, L.; Legare, P.; Kotani, A.; Parlebas, J. C. *Solid State Commun.* **1989**, *71*, 885.

(41) Mullins, D. R.; Overbury, S. H.; Huntley, D. R. *Surf. Sci.* **1997**, *409*, 307.

(42) He, H.; Dai, H. X.; Wong, K. W.; Au, C. T. *Appl. Catal., A* **2003**, *251*, 61.

(43) Borchert, H.; Frolova, Y. V.; Kaichev, V. V.; Prosvirin, I. P.; Alikina, G. M.; Lukashevich, A. I.; Zaikovskii, V. I.; Moroz, E. M.; Trukhan, S. N.; Ivanov, V. P.; Paukshtis, E. A.; Bukhtiyarov, V. I.; Sadykov, V. A. *J. Phys. Chem. B* **2005**, *109*, 5728.

(44) Reddy, B. M.; Bharali, P.; Thrimurthulu, G.; Saikia, P.; Katta, L.; Park, S.-E. *Catal. Lett.* **2008**, *123*, 327.

(45) Reddy, B. M.; Bharali, P.; Saikia, P.; Thrimurthulu, G.; Yamada, Y.; Kobayashi, T. *Ind. Eng. Chem. Res.* **2009**, *48*, 453.

(46) Reddy, B. M.; Bharali, P.; Saikia, P.; Park, S.-E.; van den Berg, M. W. E.; Muhler, M.; Grünert, W. *J. Phys. Chem. C* **2008**, *112*, 11729.

(47) Reddy, B. M.; Patil, M. K. *Chem. Rev.* **2009**, *109*, 2185.